



Construction of Novel Z-scheme Heterojunction in ZnFe₂O₄/P25 @ MOF-5 Nanocomposite from Plastic Waste for Efficient Photodegradation of Aqueous BTX Under Visible Light

Samira M. Abdel-Azim¹ · Doaa S. El-Desouki¹ · Amr H. Mady^{2,3} · Delvin Aman^{4,5}

Received: 20 August 2023 / Accepted: 26 October 2023 / Published online: 10 November 2023
© The Author(s) 2023

Abstract

An innovative strategy to reduce water pollution is adsorption-assisted photocatalysis. A novel mesoporous heterogeneous adsorbent MOF-5-based photocatalysts were successfully synthesized by a green method from plastic waste through a one-step solvothermal process. Additionally, ZnFe₂O₄ nanocrystals were physically ground with commercial Degussa P25 at room temperature to prepare ZF/P nanocomposite catalysts. These catalysts demonstrated significant photocatalytic activity for the removal of BTX from wastewater. BTX was successfully degraded in an aqueous solution utilizing integrated adsorption and photocatalytic degradation using the newly developed ZF/P@MOF-5 samples with 0.01% of ZF/P. The in-depth characterization of the ZF/P@MOF-5 confirmed its positive physicochemical properties, such as porous nature, stability, high surface area, beneficial functional groups on its surface, and photocatalytic activity. PL spectroscopy also shows that the ZF/P-incorporated MOF-5 nanocomposite has a lower electron-hole recombination rate. The as-prepared ZF/P@MOF-5 mesoporous heterogeneous adsorbent-photocatalyst presented high adsorption and maximum degradation of BTX under visible radiations after 180 min. The reusability results demonstrated that 20 P/ZF @MOF-5 composite can be used effectively for up to four cycles, which makes the process more economical. This experimental study demonstrates that the novel ZF/P-incorporated MOF-5 is a potential route to producing photocatalysts for dissociating BTX wastewater that is highly effective, stable, economical, and sustainable.

Keywords MOF-5 · ZnFe₂O₄ · BTX · P25 · Photodegradation

1 Introduction

Water contamination, mostly caused by domestic, industrial, and agricultural activities, is a major environmental issue [1–3]. Due to their relatively high solubility in water, benzene, toluene, and xylene (BTX) in particular are among the most abundant VOCs and hazardous pollutants in surface water and ground. BTX is also extremely toxic and can cause human cancer. They originate from different sources, such as petrochemical plants, paint industries, refineries, petrol stations, and oil extraction fields. In recent years, BTX has seen significant growth in use as a solvent, fuel octane booster, and leather tanner. Therefore, researchers are giving special attention to the goal of removing these aromatic molecules. Numerous studies have been conducted to lower BTX concentrations to comply with World Health Organization (WHO) standards. Various methods have been explored, such as advanced oxidation processes (AOPs),

✉ Delvin Aman
delvin.aman@epri.sci.eg

¹ Process Development Division, Egyptian Petroleum Research Institute (EPRI), Nasr City 11727, Cairo, Egypt

² School of Chemical Engineering, Yeungnam University, 280 Daehak-ro, Gyeongsan 38541, Gyeongbuk, Republic of Korea

³ Petrochemical Department, Egyptian Petroleum Research Institute, Nasr City 11727, Cairo, Egypt

⁴ Catalysis Laboratory, Refining Department, Egyptian Petroleum Research Institute (EPRI), Nasr City 11727, Cairo, Egypt

⁵ Central Analytical Laboratories, Egyptian Petroleum Research Institute, Nasr City PO Box 11727, Cairo, Egypt

adsorption, and biodegradation [4]. Photocatalysis is a well-known AOP for transforming organic contaminants into harmless by-products like CO_2 , H_2O , and mineral acids [5].

Additionally, it is safe, non-selective, economical, and compatible for treating a variety of organic pollutants [6], [7]. In contrast, photocatalyst applicability in industrial wastewater treatment is limited by low visible light absorption, high propensity for recombination of photogenerated e^- and h^+ pairs, and particle agglomeration [8]. The adsorption is a simple, economical, and highly efficient process than organic pollutants (BTX) from wastewater [9]. The pollutant cannot be degraded by adsorption; it can only be concentrated on the surface of the adsorbent. This issue can be solved by integrating the adsorption method with photocatalytic degradation. It has been demonstrated that this integration technique is effective for the treatment of pollutants even at low concentration levels, and it has the potential to become an innovation in wastewater treatment. The adsorption-assisted photocatalytic degradation mechanism typically follows the following steps: the pollutants first adsorb on the surface of the adsorbent catalyst, followed by (i) the excited adsorbate molecules that inject electrons into the catalyst's conduction band, (ii) the conduction band electrons (e^- CB) that are rummaged by O_2 to produce $\cdot\text{OH}$ radicals, and (iii) the $\cdot\text{OH}$ radicals that degrade the adsorbed molecules into harmless products [8]. The BTX from industrial waste water is eliminated or degraded via the sequential adsorption-photocatalytic oxidation process. Recent developments in functionalized metal-organic hybrid materials, known as metal-organic frameworks (MOFs), have been considered promising for application in photocatalysis and pollutant adsorptions [10]. MOFs (such as MOF-5) offer tunable organic metal clusters, a high specific surface area, a well-organized porous structure, and great hydrothermal [11]. The use of plastic waste in creating MOFs was the subject of a significant amount of studies. Our daily lives consume a lot of plastics (PET), which negatively influences the environment. Terephthalic acid, a precursor for making MOFs, has been successfully produced from recycled PET bottles. Recent research has shown that producing MOFs from BDC produced during the depolymerization of PET is an extremely appealing way to minimize production costs and environmental impact while recycling the terephthalate component of PET [12]. Since MOF-5 has a fast electron-hole recombination rate, poor light absorption in the visible spectrum, a wide energy band gap (3.88 eV), and limited adsorption capacity, its use in wastewater treatment is constrained [13], [14]. Because MOF-5 has open metal sites, which can operate as a carrier transmission route, it can be combined with semiconductors to become an effective heterogeneous semiconductor, thereby removing the difficulties associated with MOFs [15].

In this context Commercial TiO_2 (Degussa P25) has an average primary size of 21 nm and a surface area of $50 \text{ m}^2/\text{g}$, making it a standard photocatalytic material. Titania, a wide band gap semiconductor, can only absorb around 5% of the ultraviolet radiation of sunlight. On the other hand, ZnFe_2O_4 is a semiconductor with a low band gap (1.9 eV) and possible use in converting visible light [16]. However, because of its reduced valence band potential and poor photoelectric conversion capabilities, ZnFe_2O_4 cannot be used directly in the photocatalytic destruction of organic pollutants. So, TiO_2 shows relatively high reactivity and chemical stability under ultraviolet light, while zinc ferrite is sensitive to visible light [17].

In contrast to zinc ferrite, which is sensitive to visible light, TiO_2 has relatively high reactivity and chemical stability under ultraviolet radiation. Therefore, the ZnFe_2O_4 grain size is expected to provide a straightforward method for achieving effective contact between P25 and ZnFe_2O_4 and a synergistic effect in the photocatalytic process. Consequently, combining these two semiconductors may result in a novel form of composite material with high photocatalytic activity and sunlight efficiency. The creation and separation of photoexcited charge carriers can be facilitated by MOF-based semiconductors, which also have a high capacity to absorb solar energy and increased photocatalytic activity for the degradation of organic pollutants [18].

Only limited research has been conducted concerning the photocatalytic breakdown of BTX (benzene, toluene, and xylene) present in aqueous solutions. Moreover, this research has predominantly focused on utilizing visible light as the catalyst. This degradation process can occur individually or simultaneously when addressing samples in their gaseous state.

This present work is a follow-up on the sustainable, “greener” route of MOF synthesis involving the depolymerization of PET to terephthalic acid (TPA) and conversion of the latter to its organic salt linker form to metal oxide-MOF materials. Then, the effect of incorporating different weight ratios of $\text{ZnFe}_2\text{O}_4/\text{P25}$ on the properties and stability of the MOFs was studied. An integrated adsorption technique and photocatalytic degradation of BTX will also be investigated for wastewater treatment.

2 Experimental

2.1 Materials

Without additional amplification, the following analytical grade reagents were utilized in the preparation of nanocomposite: Zinc nitrate hexahydrate $\text{Zn}(\text{NO}_3)_2 \cdot 6\text{H}_2\text{O}$, (98%, Aldrich), benzene-1,4-dicarboxylic acid (BDH), PET plastic

derived), N,N-dimethyl formamide DMF, grade zinc acetate $\text{Zn}(\text{CH}_3\text{CO}_2)_2 \cdot 2\text{H}_2\text{O}$, $\text{Fe}(\text{NO}_3)_3 \cdot 9\text{H}_2\text{O}$, NaOH, NaCl and P25(commercial).

2.2 Organic Linker (1, 4 Benzene Dicarboxylic acid/terephthalic acid/BDC) from Waste PET Plastic

The waste poly (ethylene terephthalate) (PET) plastic has been chemically recycled to produce high-purity terephthalic acid (TPA) [19]. Waste PET plastic needed pretreatment first. PET water bottles used previously were collected, and the rings, labels, and caps were removed. The PET bottles were manually cut into 1 cm x 1 cm flakes, rinsed five times with deionized water, and dried. Alkaline hydrolysis was then employed to pretreat waste PET plastic. 5.6 g of NaOH were dissolved in 125 ml distilled water to prepare (1 M) NaOH. PET flakes (50 g, 0.26 mol) were then immersed in the solution. Transfer the obtained mixture to the autoclave reactor. The PET decomposition temperature was set at 170 °C for five hours. The reactor was then allowed to cool to ambient temperature spontaneously, yielding disodium terephthalate salt (TPA- Na_2). Then, neutralizing the reaction mixture filtrated with 5 M H_2SO_4 , as demonstrated in Scheme 1, yields pure TPA. Finally, the resulting TPA was weighed after being dried in an oven at 80 °C.

2.3 Preparation of MOF-5 Using Organic Linker (BDC) Derived from Waste PET Plastic

Zn-MOF-5 was synthesized using solvothermal according to a previously reported method with minor modifications [20]. 4.24 g of Zinc nitrate hexahydrate ($\text{Zn}(\text{NO}_3)_2 \cdot 6\text{H}_2\text{O}$, 98%) and 1.26 g terephthalic acid (TPA), which we prepared from plastic waste were dissolved in N, N-dimethylformamide (DMF). After stirring for up to two hours to achieve homogeneity, this mixture was sealed in a Teflon-lined solvothermal tank and heated to 170 °C for seven hours, producing a solid white precipitate. After being gradually cooled to ambient temperature, it was centrifuged at 7000 rpm for 15 min. The white product was washed with DMF, vacuum-dried overnight at 60 °C, and then placed in a desiccator for storage.

2.4 Preparation of ZnFe_2O_4 Nanoparticles (ZF)

By the solid-state reaction of inorganic precursors, ZnFe_2O_4 (ZF) was prepared [16]. Analytical grade

$\text{Zn}(\text{CH}_3\text{CO}_2)_2 \cdot 2\text{H}_2\text{O}$, $\text{Fe}(\text{NO}_3)_3 \cdot 9\text{H}_2\text{O}$, NaOH, and NaCl were mixed in a molar ratio of (1:2:8:2). After that, mix everything in an agate mortar for around 30 min. The mixture gradually changed color as the reaction proceeded, going from colorless after 3 min to bright red after 1 min, then brown after 10 min. The mixture was repeatedly rinsed with deionized water. The powders were dried at 80 °C for 2 h after being washed to remove any remaining sodium chloride. Then, the powders were calcined for 2 h at 700 °C.

2.5 Preparation of ZnFe_2O_4 /P25 Nanoparticles (ZF/P)

By using a grinding technique, ZF/P nanocomposites were synthesized at different weight ratios of ZnFe_2O_4 :P25 (90:10, 80:20, 70:30, 10:90, 20:80, and 30:70). For 10 min, the dry mixture was physically strong continuous grinding. The mixture was then dried for 1 h at 200 °C. The prepared catalysts were named as 10P/ZF, 20P/ZF, 30P/ZF, 10ZF/P, 20ZF/P and 30ZF/P, respectively.

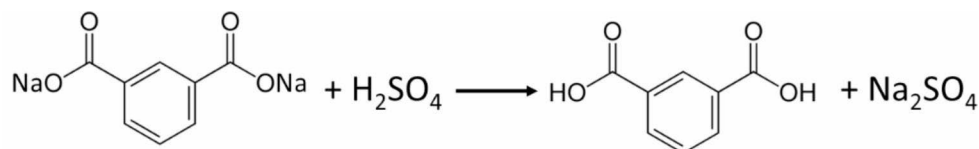
2.6 Incorporation of ZnFe_2O_4 /P25 Nanoparticles to the MOF-5

To incorporate different weight ratios of ZF/P (80:20 and 20:80) nanoparticles into MOF-5, a certain amount of the ZF/P nanoparticles added to the mixture of $\text{Zn}(\text{NO}_3)_2 \cdot 6\text{H}_2\text{O}$, TPA and DMF in the autoclave. Then the same sequence of the MOF-5 preparation was performed. These prepared catalysts were named as 20P/ZF@MOF-5, and 20ZF/P@MOF-5, respectively.

2.7 Characterization of the Catalysts

There are several techniques were used to characterize the synthesized samples. X-ray diffraction (XRD) on (a Shimadzu XD-1, Japan) diffractometer, Employing Cu Ka radiation ($\lambda = 0.1542$ nm) at a beam voltage of 40 kV and a current of 40 mA, the crystallinity and phases of produced samples were examined. The Joint Committee on Powder Diffraction Society's (JCPDS) database indexed the XRD peaks. By using Scherrer's equation, the average crystallite size was estimated. $D = K\lambda / \beta \cos\theta$, Where D is the crystal size in nm, θ is the diffraction angle, K is a constant taken as 0.89, $\lambda = 0.15406$ nm, and β is the broadening of the diffraction line measured at half maximum intensity. Fourier-Transform Infrared Spectroscopy (FTIR) analysis

Scheme 1 Pure TPA is produced by neutralizing the PET alkaline hydrolysis reaction mixture using conc. H_2SO_4



was conducted within the 400–400 cm^{-1} transmission range using the (PerkinElmer spectrometer, USA) model 100 series. An NMR study was conducted to determine the purity of the produced TPA using a mercury (VX-300 NMR, USA) spectrometer. At the ambient temperature in dimethyl sulphoxide (DMSO-d_6), the carbon-13 (^{13}C) spectra were run at 75.46 MHz, and the proton-nuclear magnetic resonance (^1H NMR) spectrum was at 300 MHz. Chemical shifts were quoted in δ and related to that of the solvents. Raman spectra were conducted using a SENTERRA Dispersive Raman Microscope (Bruker, USA) equipped with a diode Nd: YAG laser from 10 to 2000 cm^{-1} at ambient temperature and a wavelength of 532 nm Thermo Fisher Scientific's KALPHA (Thermo Fisher Scientific, Waltham, MA, USA) was used to collect information regarding X-ray photoelectron spectroscopy (XPS) utilizing monochromatic X-ray Al K-alpha radiation with a spot size of 400 μm at a pressure of 10–9 mbar and pass energies of 200 eV for the whole spectrum and 50 eV for the narrow spectrum. The nitrogen adsorption-desorption isotherm was recorded by a gas sorption analyzer Quantachrome NOVA2000, USA, at 77 K. Before measurement, the sample was degassed under vacuum at 120 $^\circ\text{C}$ for 12 h. As well, by using the spectrofluorophotometer RF-5301PC (Shimadzu, Japan) with an excitation wavelength of 300 nm, photoluminescence spectra (PL) were measured. A diffuse reflectance attachment IRS-2200 (Shimadzu, Japan) was utilized with a UV-vis spectrophotometer (Jasco model V-570). A field emission scanning electron microscope (FE-SEM) and energy-dispersive X-ray spectroscopy (EDX) analysis (Zeiss, Sigma 300VP, Germany) were utilized to examine the external morphology of the prepared catalysts. The samples were analyzed using a Transmission Electron Microscope (TEM, Model JEM-200CX, JEOL, USA).

3 Photocatalytic Reactions

Photocatalytic reactions occurred using the homemade photo cylindrical reactor, using a 150 W Xenon lamp (400–480 nm, λ_{max} 450 nm). The experiments continued with stirring and cooling by water circulation at 25 $^\circ\text{C}$. An aqueous solution containing benzene, toluene, and xylene (10 ppm each) was used in this study. 0.002 g of the as-synthesized catalyst was added in 200 ml of 10 ppm BTX solution. Then, this suspension was stirred in the dark at room temperature for 30 min to obtain equilibrium between the adsorption and desorption of the BTX molecules at the catalyst surface. After dark time, the BTX solution was exposed to an Xenon lamp for up to 180 min. At regular intervals, 20 μl of BTX aliquots were collected with a syringe to evaluate the reduction in BTX concentration due to the

integrated adsorption and photocatalytic reactions using an HPLC instrument (HPLC model Agilent 1200 series) with UV-vis detector Waters 2410 Isocratic pump. The C-18 column was used as a stationary phase, and the mobile phase was a mixture of methanol/water with a ratio of 70/30 and a flow rate of 1 ml/min at room temperature. To assess the recyclability and stability of the photocatalyst, the most efficient catalyst among those prepared was employed continuously for five cycles. After each cycle, the solution was decanted, and fresh polluted water was added to the catalyst without any washing.

4 Results and Discussion

4.1 X-ray Diffraction (XRD)

The typical diffraction patterns of as-prepared ZnFe_2O_4 (ZF) and with different percentages of commercial P25 10, 20 or 30% P/ZF & 10, 20 or 30% ZF/P are shown in S 1. All mixtures have ZnFe_2O_4 in the spinel cubic structure, which was confirmed by all of the diffraction peaks 30.1, 35.3, 42.8, 53.2, 56.6, and 62.2 $^\circ$ which matched with the standard JCPDS (Card No. 22-1012) [20]. The strong, sharp peaks showed that ZF nanoparticles were well crystallized. For the impure phase of ZnO, a weak peak was discovered at 31.7 $^\circ$, found in higher intensity in the 10P/ZF sample [21]. Also, two small peaks are found at 25 and 34 $^\circ$, indicating a very small amount for the impure phase of Fe_2O_3 [22]. Furthermore, XRD spectra for ZF/P composites show only the rutile TiO_2 (P25) peaks with strong intensities and ZnFe_2O_4 peaks with weak intensities and vice versa for P/ZF samples. It is noted that there are no peaks for the anatase phase in the composites. The absence of peaks may be due to a small iron oxide fraction. The report supports these results [23], [24] reported that the low iron oxide content deduced the transformation of anatase to a rutile phase [25]. It can be explained by the fact that the Fe^{3+} radius is similar to that of Ti^{4+} , so it is favorable for iron substitution in the matrix of TiO_2 . This process facilitates the transformation of anatase to rutile at a low temperature [26]. Also, the phase transformation of anatase to rutile can happen in a dry medium condition during mechanochemical synthesis at different temperature points inside the grinding vessel [27].

Figure 1 illustrates the XRD pattern of the prepared MOF-5, revealing distinct crystal peaks corresponding to crystal planes (220), (400), (420), (531), (533), (551), (751), and (911) at 2θ values of 8.54, 13.55, 15.30, 20.59, 22.36, 24.71, 31.31, and 32.13, respectively. These results confirm the successful synthesis of crystalline MOF-5 using the solvothermal technique [28]. Many peaks between $2\theta \sim 31$ and 37 $^\circ$ prove the presence of the ZnO phase [29]. All the

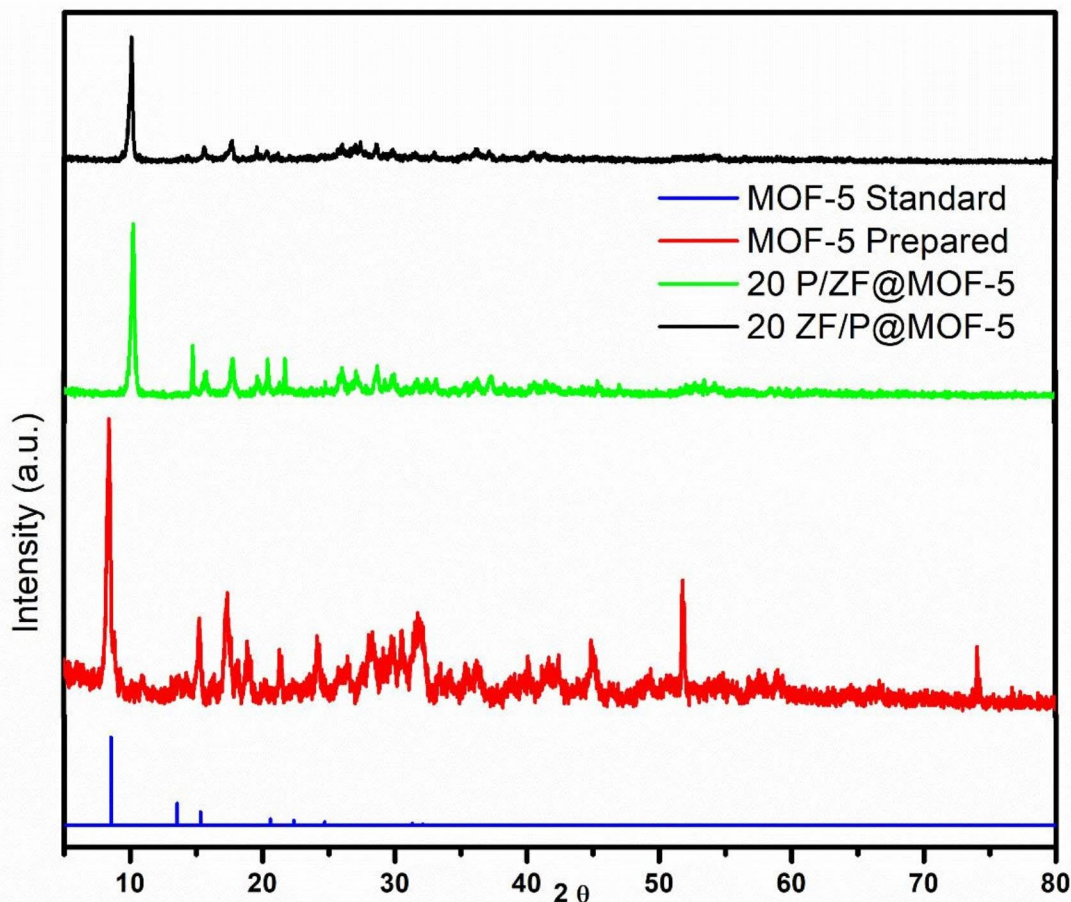


Fig. 1 XRD pattern of MOF-5, 20 P/ZF@MOF-5 and 20 ZF/P@MOF-5

distinctive peaks of ZF, P25, and MOF-5 are shown after loading ZF/P or ZF/P on MOF-5. There is no appearance of new peaks in the XRD patterns, indicating the separation of P25, ZF, and MOF-5 crystalline phases [21]. The XRD patterns of composites show that the peaks of Zn-MOF have strong intensities, whereas ZF and P25 peaks have weak intensities. This observation can be attributed to the low proportion of ZF and P25 in the composites (0.01%). From the above result, we can deduce that ZF/P or P/ZF diffused into the MOF-5 pores. The average crystallite sizes of the prepared samples composites are calculated using the Scherrer equation to be about 30, 57, 51, 81, and 99 nm for ZF, MOF-5, 20ZF/P, 20P/ZF, 20P/ZF@MOF-5 and 20ZF/P@MOF-5, respectively.

4.2 Fourier Transform Infrared Spectroscopy

FTIR spectra of all as-prepared catalysts were characterized within the wavenumber range of 400–4000 cm^{-1} . We found that the TPA produced from waste plastic by

alkaline hydrolysis of PET was similar to the standard commercial TPAs and identified it as terephthalic acid from its FTIR spectra (S.2) [20]. The characteristic bands of the aromatic dicarboxylic acids are located at 3070 cm^{-1} for $\nu\text{C-H}$ aromatic, 1677 cm^{-1} for $\nu\text{C=O}$, and 1282 cm^{-1} for $\nu\text{C-O}$. Additionally, the 1, 4-disubstituted benzene ring corresponds to the 1509, 1572, and 1136 cm^{-1} bands. These remarks are confirmed by Proton nuclear magnetic resonance (^1H NMR) and ^{13}C carbon nuclear magnetic resonance (NMR) shown in the supplementary part (S.3).

The FTIR spectra for the prepared ZF, 20ZF/P, and 20P/ZF are shown in S4. Water molecules are found on the surface of ZF, as evidenced by the broadband absorption peak centering at 3446 cm^{-1} . The 542 and 467 cm^{-1} vibration peaks correspond to Fe-O and Zn-O for ZF's tetrahedral and octahedral modes, respectively [30], [31]. A shoulder band observed at 676 cm^{-1} is explained by the cation exchange between the tetrahedral and octahedral spinel sites that often occur in zinc ferrite [32]. The O-H bending contributes to an additional vibration band located at 1643 cm^{-1} [33]. These

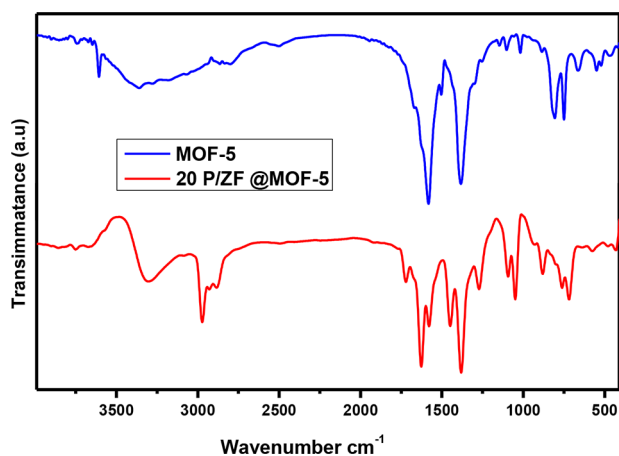


Fig. 2 FT-IR spectra of MOF-5 and 20P/ZF @ MOF-5.

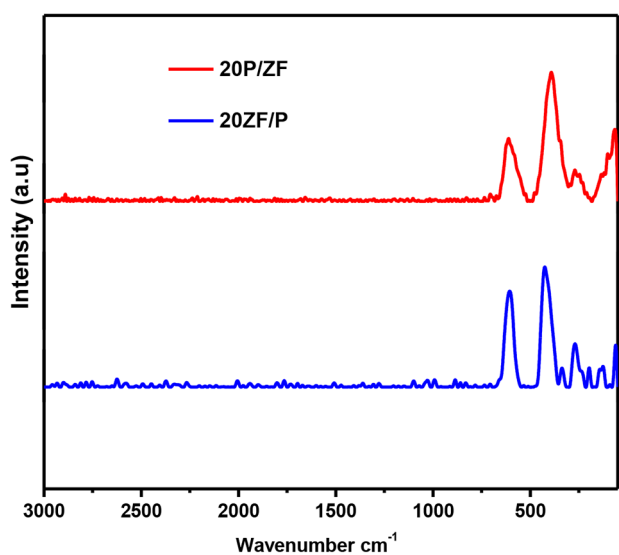


Fig. 3 Raman spectroscopy for the prepared 20ZF/P and 20P/ZF.

findings confirm the successful synthesis of high-purity Zn-ferrite (ZF).

Figure 2 illustrates the FT-IR spectra of MOF-5 nanoparticles synthesized using the solvothermal method and TPA we produced from plastic waste. The stretching vibration of the Zn-O bonds in the tetrahedral coordinated Zn_4O cluster exhibits many peaks between 400 and 1000 cm^{-1} [34]. Two sharp peaks observed at 806 and 749 cm^{-1} are related to the presence of the C-H group in the benzene ring of terephthalic acid [35]. The presence of two prominent vibration bands at 1593 and 1383 cm^{-1} can be attributed to the asymmetric and symmetric stretching vibrations of carboxylic (COO) groups, respectively. The sharp and broad peak in the range of 1658 to 1500 cm^{-1} is allocated to the stretching vibration of the C-O bond linked to Zn, confirming the attachment of the aromatic ring of terephthalic acid to Zn_4O [36]. The bands at 2350 and 2500 cm^{-1} are due to the C-H

stretching vibration of the methylene group in DMF molecules [37]. The broadband between 3000 and 3600 cm^{-1} is assigned to the OH of carboxylic acid.

4.3 Raman Spectroscopy

Figure 3 depicts the Raman spectroscopy for the prepared 20ZF/P and 20P/ZF. For the ZF sample, three different spectral intervals with poor resolution can be recognized in the regions 600–750, 410–550, and 270–370 cm^{-1} . The Broad bands centered at 350 and 660 cm^{-1} for the F_{2g} and A_{1g} modes, respectively [38]. These bands correspond to the ZF vibrational modes of the cubic nanoparticles. As expected, Raman spectra for 20 F/P and 20P/ZF show the existence of ZF peaks and P25. While the bands of rutile TiO_2 dominate in 20 ZF/P catalysts, ZF bands dominate in the 20 ZF/P. There are five active Raman modes ($A_{1g} + E_g + 3F_{2g}$) for the cubic spinel structure of ZF belonging to the space group $Fd3m$ [39]. The octahedral sites (BO6) are characterized by a peak at 245 cm^{-1} related to the Raman mode of E_g symmetry [39]. The strong band at 611 cm^{-1} corresponds to the A_{1g} mode of oxygen atoms at the tetrahedral sites (AO_4) [40]. According to many authors, in the cubic spinels, including ferrites, the modes above 600 cm^{-1} mostly correspond to the motion of oxygen in tetrahedral AO_4 groups, and peaks between 410 and 550 cm^{-1} are attributed to the vibrations of Fe–O and Zn–O bonds at the octahedral sites [41–43]. Furthermore, many additional peaks between 200 and 400 cm^{-1} are detected, confirming the presence of the hematite phase [44]. A band at 437 cm^{-1} was also recognized as the E2 mode of the remaining zinc oxide [40], [41]. These results are compatible with the XRD analysis (S.1). On the other hand, the typical Raman bands originating from the rutile phase of TiO_2 (P25) appear at 143, 235, 455, and 612 cm^{-1} for B_{1g} , E_g , and A_{1g} modes, respectively [45], [46]. The catalysts exhibit a higher proportion of P25, resulting in more pronounced peaks associated with the rutile phase. The XRD and Raman techniques analyses provide solid evidence for forming a pure rutile phase in the TiO_2 .

4.4 X-ray Photoelectron Spectroscopy

XP spectra were obtained to examine binding energy distribution across various energy levels and explore the elemental states. Figure 4a–e displays the survey scan and deconvoluted spectra for all prepared catalysts. The XP survey scan shows spectral binding energies of different zinc, carbon, and oxygen orbitals. The strong intensity peaks observed at binding energies of 1043.88 and 1020.98 eV can be associated with the $2p_{1/2}$ and $2p_{3/2}$ levels, respectively, as depicted in Fig. 4b. This reflection confirms the presence of Zn (II)

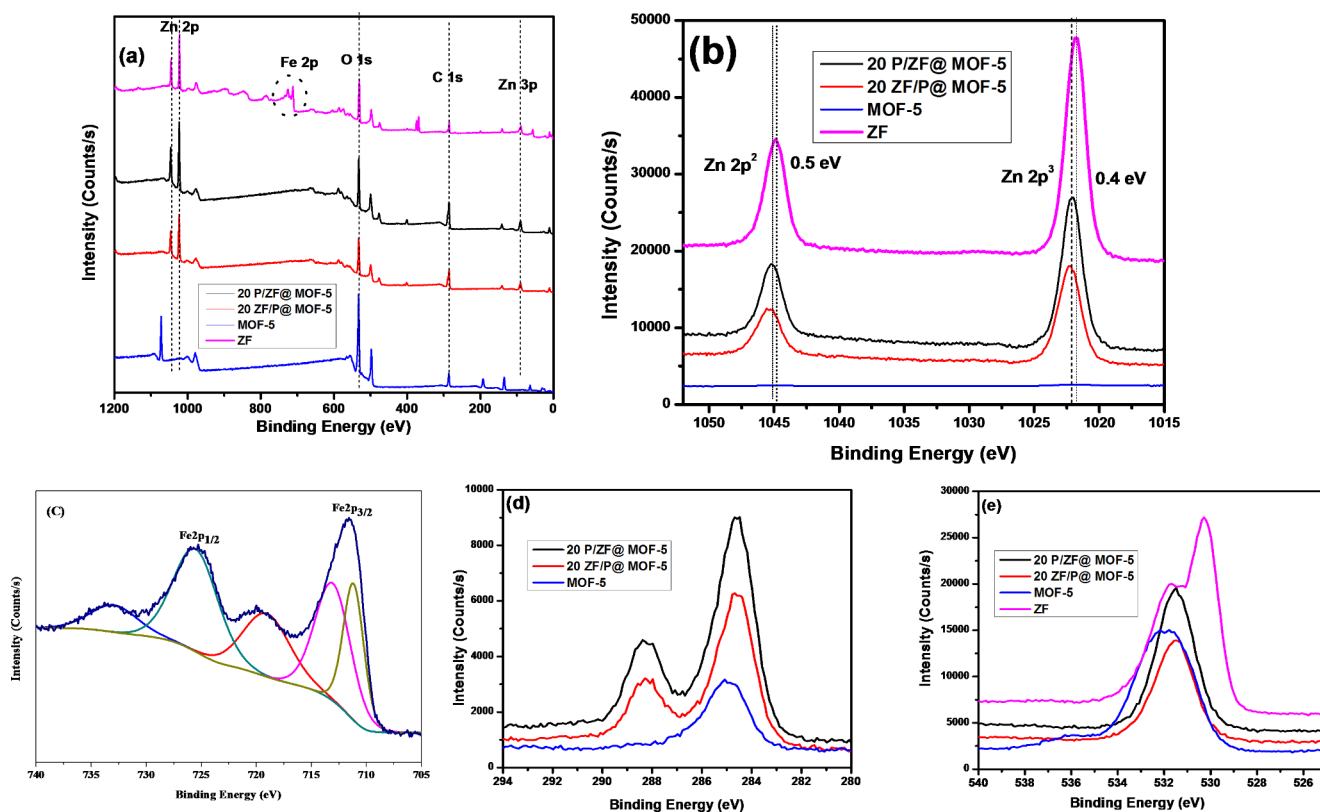


Fig. 4 XPS spectra of (a) survey spectra; deconvoluted XP spectra of (b) zinc 2p, (c) iron 2p, (d) carbon 1s, and (e) oxygen 1s

in the oxidation state within ZF [47]. The lack of identical peaks in the MOF-5 spectra is ascribed to the absence of unbound metal ions on the surface structure. The sharp peak at 978.39 eV in the XP spectra of MOF-5 resembles the presence of free Zn^{2+} ions on the framework topology.

Furthermore, zinc-deconvoluted X-ray photoelectron spectra reveal shifts in binding energy values and diminished peak intensities, which could be attributed to the binding interactions involving ZF/P and P/ZF nanoparticles [28]. According to the Fe 2p spectra (Fig. 4c), the tetrahedral and octahedral sites were represented by binding energies for Fe $2p_{3/2}$ of 713.1 and 711.4 eV, respectively [48]. This result agrees with the FTIR data. However, the peak at a binding energy of 725.6 eV is consistent with the Fe $2p_{1/2}$, and the two shake-up satellite signals (at 719.3 and 732.8 eV) also indicated that only Fe^{3+} was present in the ZF sample [49]. These results confirmed that the state of Fe in the samples 20 P/ZF and 20 ZF/P is Fe^{3+} oxidation status. The non-appearance of identical peaks in the spectra of 20 P/ZF@MOF-5 and 20 ZF/P@MOF-5 is linked to the lack of available iron ions on the surface structure, which could have been utilized for forming bonds with the MOF-5 particles. However, the O 1s binding energy of 530 eV in the ZF sample was assigned to lattice oxygen binding with Fe and Zn (represented as Fe–O, Ti–O, and Zn–O) [17]. The intense peak at a BE value of 285 eV corresponds to the

existence of 1s orbitals of carbon atoms of the terephthalate framework structure [50]. The binding energy of O 1s in MOF-5 is changed from 532 to 531.5 eV when loading with ZF/P, and P/ZF occurs onto the framework structure, further confirming the interaction and composites formation [51].

4.5 Nitrogen Adsorption-desorption Isotherm

To study the surface area and the pore size distribution of the catalysts, nitrogen adsorption–desorption isotherm was performed for pristine and 20P/ZF incorporated MOF-5 (Fig. 5). The adsorption isotherm belongs to the type II isotherm, indicating the existence of both micropores and mesopores structure materials with a relatively high surface area [50]. With increasing adsorption pressure, the first inflection point of the isotherm rapidly appears, indicating that monolayer adsorption is completed. Multilayer adsorption gradually occurs as the adsorption pressure increases at $P/P^0 < 0.9$. When P/P^0 approaches unity, a steep increase in the isotherm occurs, and the adsorption layer is infinite [51], [52]. The specific surface areas exhibit minimal variance; the MOF's surface area decreases from 450 to 448 m^2/g , and the pore volume reduces from 0.051 to 0.043 cm^3/g after incorporating 0.01 wt% of 20P/ZF. Figure 5 (inset shows the pore size distribution), where micro- and mesopores are shown in the two samples. It is worth noting that both

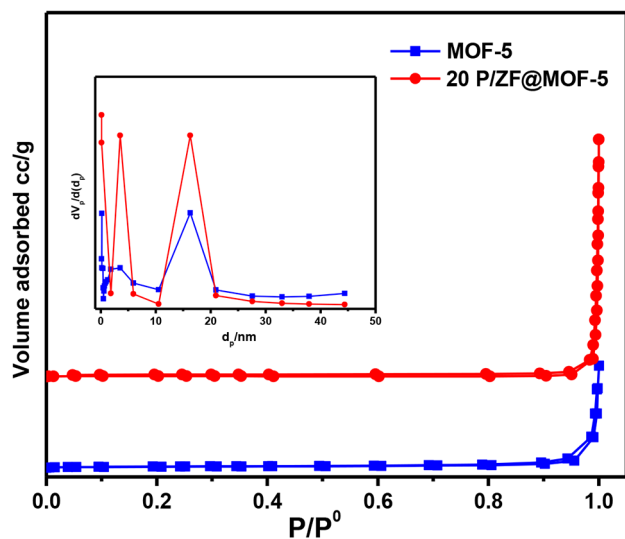


Fig. 5 N_2 adsorption–desorption isotherms of the MOF-5 and the 20P/ZF@MOF-5 nanocomposite, inset: pore size distribution

samples have the same number of peaks, but the amount of micro- and mesopores has increased after 20P/ZF incorporation into MOF-5 (about 4 and 2 times, respectively). The mesoporosity and relatively large surface area significantly influence the adsorption properties of the prepared sample.

4.6 Photoluminescence Analysis

The charge carriers' recombination and carrier trapping processes have been studied using the photoluminescence (PL) spectra. The PL obtained for 10 and 30ZFP & 10, 30P/ZF catalysts were characterized between 500 and 600 nm at an excitation wavelength of 345 nm (S.5 a & b). All of the produced catalysts had a single broad emission peak. A well-defined peak was seen in the spectra at 498 nm, which can be attributed to inter-band (CB-VB) radiation recombination. This main peak is a prominent and distinctive emission peak for catalyst recombination, emitting light with an energy equal to or slightly higher than the band gap of photocatalysts. The intensity of this emission peak is significantly changed. The intensities of this peak for 10, 20, 30P/ZF and 10, 20 and 30ZF/P catalysts are 192.09, 178.12, 192.09, 354.14, 215.72, and 305.05, respectively. It is well known that, during grinding processes, a linked semiconductor system (nanocomposite) is believed to emerge between ZF with a narrow band-gap energy (2.1 eV) and P25 with a broad band-gap energy (3.9 eV).

Moreover, in unsaturated hanging bonds, the ZF and P25 particles interact sufficiently, creating a synergistic effect in the photocatalytic process [53]. The grinding method we utilized minimizes the difficult colloid process and significant energy consumption of mechanochemical ball milling. On

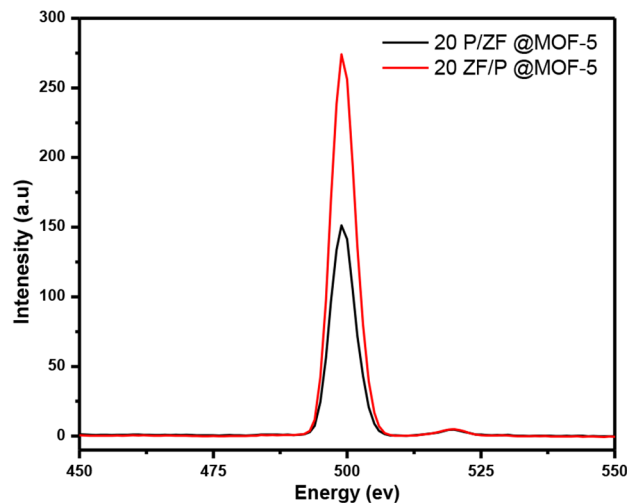


Fig. 6 PL spectra of 20 ZF/P @ MOF-5 and 20P/ZF @ MOF-5.

the other hand, as depicted in Fig. 6, the photoluminescence spectra of 20P/ZF@MOF-5 and 20ZF/P@MOF-5 had the same strong peak at 498 nm with the intensities 151.21 and 274.11, respectively. According to the above values of band gap energy of all currently prepared catalysts, we can confirm that the presence of ZnO phase in the 20P/ZF@MOF-5 and 20P/ZF (as depicted from XRD analysis) may act as a separation centre [54].

4.7 UV–Visible Spectroscopy

Figure 7 displays the samples' UV–visible diffuse reflectance spectra in their as-prepared state (20P/ZF@MOF-5, 20ZF/P@MOF-5, 20P/ZF and 20 ZF/P). The optical properties of the currently prepared samples were determined using UV-vis spectroscopy in the range of 200–800 nm. The band gap can be determined using the equation $\alpha h\nu = k(h\nu - E_g)^{1/2}$ where α , h , ν , E_g , and k represent the absorption coefficients, Planck's constant, light frequency, band gap, and a constant, respectively [55]. The estimated E_g values of the as-prepared 20P/ZF @MOF-5, 20ZF/P@MOF-5, 20P/ZF and 20ZF/P samples were estimated to be 2.5, 3, 3.1, and 3.2 eV, respectively, which indicate that all the above samples would possess photocatalytic ability under visible light irradiation. These samples' lower E_g values are beneficial for increasing light absorption and photocatalytic efficiency [56]. In addition, all composites have spectral structures that are quite similar. Also, all samples have a visible light response range, and the UV-vis spectra absorption bands below 700 nm are attributed to organic ligand-to-metal charge transfer (LMCT) and the d-d transition of octahedral ZF [57]. Furthermore, it is worth noting that the band gap energy is decreased and the absorption edge of the MOF-5 composite is slightly red-shifted when loaded with P25 and

Fig. 7 UV–Vis diffuse reflectance spectra (a) of all samples and (b) the relationships between $(\alpha h\nu)^2$ and photo energy ($h\nu$)

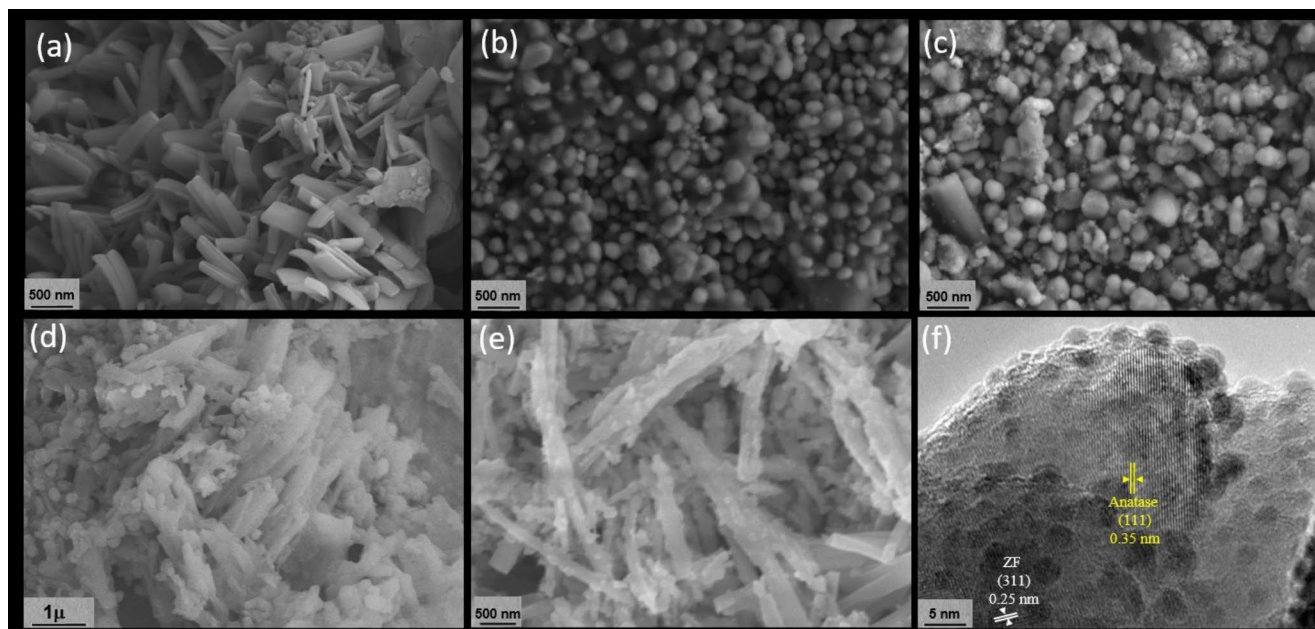
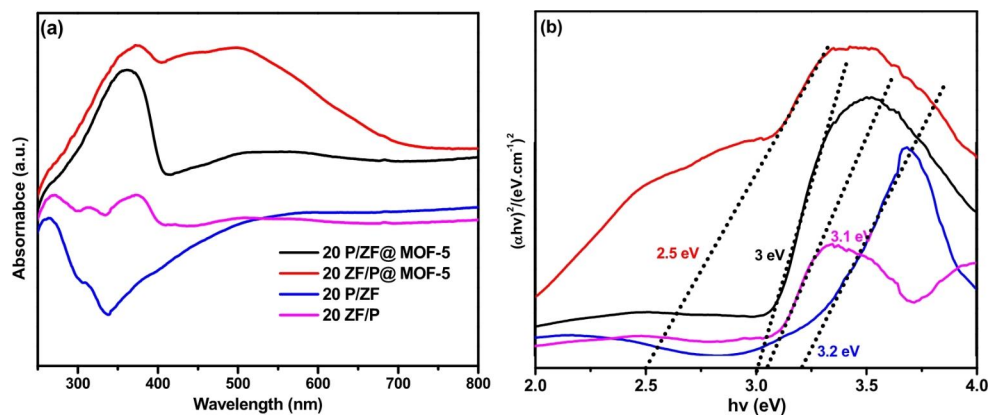


Fig. 8 FE-SEM images (a) as-prepared MOF-5, (b) 20ZF/P, (c) 20P/ZF, (d) 20ZF/P@MOF-5, (e) 20P/ZF@MOF-5, and (f) HR-TEM of 20P/ZF@MOF-5

ZF. The UV–visible light spectrum of the composite photocatalyst, 20P/ZF@MOF-5, indicates that the visible light absorption intensity is significantly the highest one, which can be attributed to the intensive absorption of UV–visible light by the ZF/P nanoparticles in the MOF-5 structure.

4.8 Scanning and Transmission electron Microscopy Analysis

SEM and TEM measurements were used to improve both the morphology and microstructure of the synthesized ZF. Fig S6 displayed SEM images of ZF nanoparticles. It was found that the crystalline grains had high porosity and very uniform shape morphology [58]. According to the TEM image magnified of ZF (S.6), the nanoparticles were between 10 and 20 nm in diameter and had slight aggregation [59]. From image, the big particles are composed of

aggregated small particles. The magnetic attraction forces of ferrite may be responsible for particle aggregation [60].

The morphology and particle size of the MOF-5, 20P/ZF, 20ZF/P, 20ZF/P@MOF-5 and 20P/ZF@MOF-5 catalysts are investigated (Fig. 8). MOF-5 crystal structures in multiple dimensions are displayed. Non-agglomerated, regular, with rectangular crystals are observed in the FE-SEM image (Fig. 8a) [35]. According to Akbarzadeh et al., the non-agglomerated morphology of MOF-5 was the result of proper bonding between linker and metal [61]. On the other hand, almost uniform edged round shapes with dispersed aggregation of 20ZF/P and 20P/ZF are shown in the FE-SEM images (Fig. 8b and c) the diameter of the particles is ~ 100 nm. It is noted that, the particles of 20ZF/P are more regular and round than the 20P/ZF particle. As shown in Fig. 8d and e, the morphological structure of 20P/ZF@MOF-5 and 20ZF/P@MOF-5 catalysts showed regular

morphologies of ZF/P particles well dispersed on the surface of the maintained MOF-5 skeleton which confirmed by the HR-TEM Fig. 8f. Figures in S.6b shows the 20P/ZF @ MOF-5 images at different scales to more illustrate its morphology. The chemical composition for prepared MOF-5, ZF/P and P/ZF samples was examined using the EDS spectra (S.7). In case of MOF-5, the only elementary components that depicted as strong peaks are for zinc, carbon, and oxygen. For other composites, the elementary components of the composite showed weak peaks for Ti and Fe which refers to the small amount and the well dispersion of 20P/ZF into MOF-5 pores.

4.9 Adsorption and Photocatalytic Activity Performance

In order to investigate the adsorption and photocatalysis of 20P/ZF@MOF-5, 20ZF/P, 20P/ZF and MOF-5 composites, different processes such as photolysis with or without the photocatalysts, and adsorption tested in the dark at room temperature were conducted and the results are shown in (Fig. 9). As found from the results of photocatalysis of BTX in the solution and under the visible light, the removal of BTX could be ignored as nearly no degradation occurred for 180 min. As for the adsorption process after 30 min, the amount of BTX adsorbed onto 20P/ZF@MOF-5 (Fig. 9R1a) and MOF-5 (Fig. 9R4a) without visible light was higher than that of 20ZF/P and 20P/ZF (Fig. 9R2a and R3a, respectively). This result is mostly attributed to the high surface area of 20P/ZF@MOF-5 (448 m²/g) and MOF-5 (450 m²/g). Combining photocatalysts with adsorbents would synergize the dual advantages of each component [62], [63]. The degradation of BTX by 20P/ZF@MOF-5 under visible irradiation (Fig. 9R1b) demonstrated that there were significant synergistic effects of adsorptive properties and photocatalytic activity of this photocatalyst. We noted that the 20P/ZF@MOF-5 had relatively higher photodegradation efficiency for BTX under visible light irradiation as compared with other materials. In the absence of MOF-5, the results confirmed the less adsorption effect of toluene and xylene although those catalysts showed also complete degradation of BTX contaminants. But from the economic point of view, we can see that the cost used in experiments R2 and R3 are too high because using two different types of metal oxides compared to the composite R1 which contains very less load of the metal oxides (0.01% ZF/P). So maximizing the benefit of using un-biodegradable waste (drinking bottles) and using it in the preparation of MOFs, then decorating it with a very less amount of metal oxide to achieve high photocatalytic efficiency has an economic impact.

Also as shown in Fig. 10 the nanocomposite exhibits no obvious reduction in the photocatalytic degradation efficiency after five cycles. This indicates the possibility of using the catalyst for a longer operation time. An exhaustive explanation of these results is not easy because the photoactivity depends on bulk, surface physicochemical, and intrinsic electronic properties of the catalysts; in principle, these last can be positively modified for the coupled ZF/P with MOF-5 as a dual Z-scheme mechanism. This phenomenon increases the availability of the pairs on the surface of the photocatalyst and consequently, an improvement of the occurrence of redox processes can be expected.

The FTIR spectrum of the 20P/ZF@MOF-5 catalyst after 30 min dark, 1 and 3 h irradiation time for the photocatalytic degradation of BTX is shown in Fig. 11 it is clear that some photocatalytic oxidation products are deposited on the surface. In the fresh catalyst, a strong broad peak in the region from 3000 cm⁻¹ to 3400 cm⁻¹ is related to O-H vibration stretching of all hydrogen bonded in hydroxyl groups [64]. This peak is increased after 30 min in the dark, then decreased gradually till almost vanished after 3 h irradiation. This indicates the adsorption of the BTX molecules on the surface of the catalyst at a dark time, meanwhile degrading after irradiation and breaking down into simple compounds. Also, many broad bands in this region are overlapped with C-H of aryl stretching vibration groups after the reaction time [65]. The bands detected at 2975 and 2880 cm⁻¹ are assigned to the C=C stretching in the aromatic rings. The sharp peak at wavenumber 1600–1700 cm⁻¹ and centred at 1630 cm⁻¹ is due to the carbonyl (C=O) stretching vibration of aryl carboxylic acids. Bands from 1000 to 1100 cm⁻¹ and from 650 to 770 cm⁻¹ are for the C-H deformation vibration [66]. The presence of C=O and O-H stretching vibration bands are indicative of the carboxylic acids. The peak observed at 3094 cm⁻¹ is characteristic of =C-H vibration of aromatics [65]. After 3 h irradiation, this peak disappeared, indicating the absence of aromatic compounds on the surface of the catalyst. On the other hand, the appearance of the peaks at a slightly lower frequency than =C-H of aromatics (below 3000 cm⁻¹) are for -CH stretching of alkane [67]. This result improves the decomposition of aromatic compounds of pollutants into aliphatic compounds. Furthermore, the absorption bands in the regions 1440–1500 and 1570–1600 cm⁻¹ are due to C-C stretching vibrations in the aromatic ring [65]. It is clear that these peaks are increased in the dark on the catalyst surface and decreased gradually after 1 h (S.8), then become very small after 3 h irradiation. This result also indicates the photodegradation of BTX compounds after adsorption in the dark to other simplest compounds. Two peaks from 675 to 900 cm⁻¹ for the out-of-plane or C-H bending bands are also characteristic of the aromatics [64]. It is clearly noted

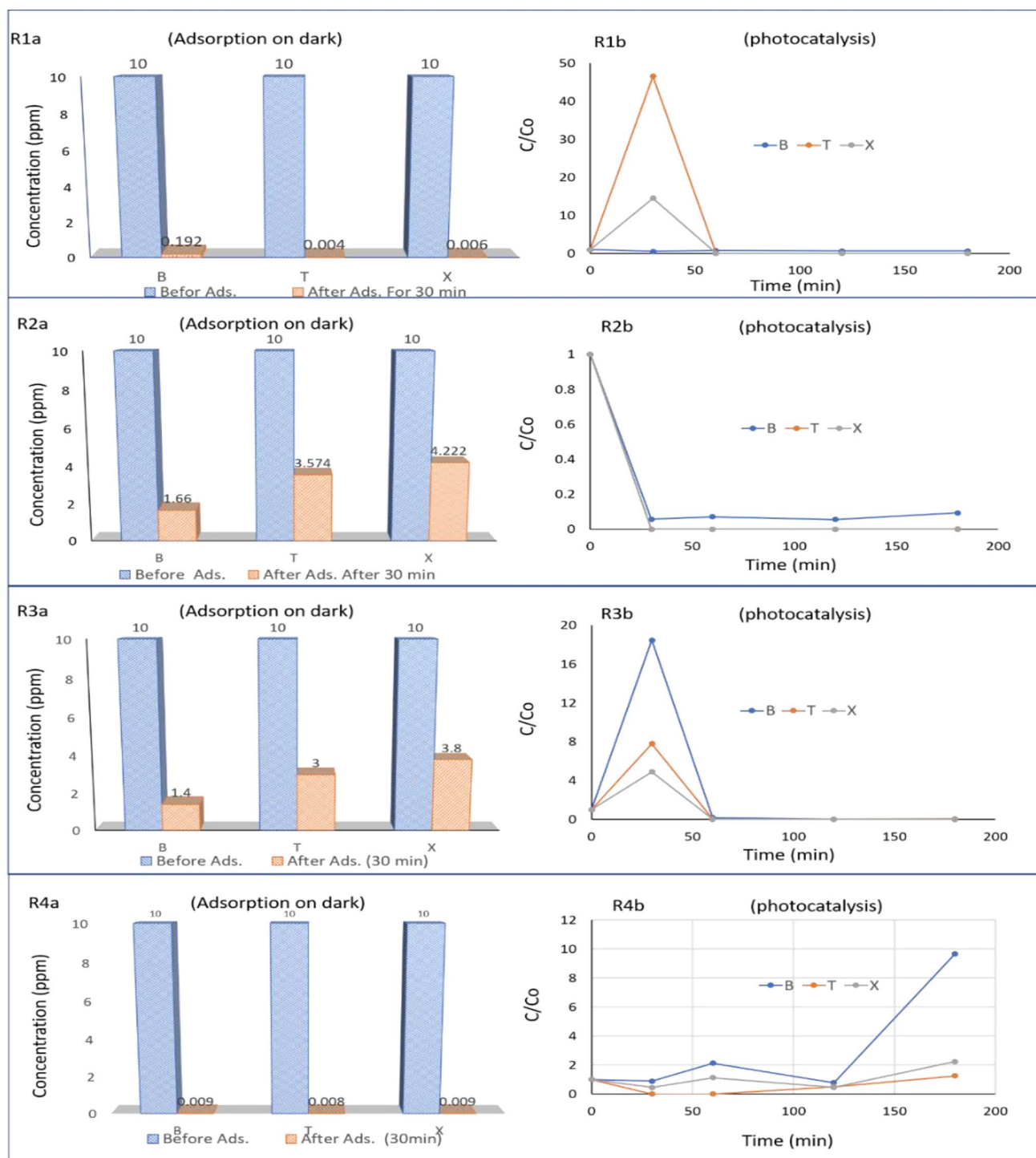


Fig. 9 Adsorption activity (R1 a, R2 a, R3 a and R4 a) and photocatalytic activity (R1 b, R2 b, R3 b and R4 b)

that the peaks related to the aromatics that are present in the FTIR pattern of the fresh catalyst are due to the presence of aromatic rings in the catalyst structure. But, the intensity of these peaks is increased in the dark sample, indicating the deposition of aromatic pollutants (BTX) on the surface of the catalyst. The presence of these peaks and other peaks

related to the aryl group below 3000 cm^{-1} indicates the decomposition of aromatics on the catalyst surface and the formation of aliphatic compounds. After 3 h irradiation, all the characteristic aromatic peaks almost disappeared from the surface of the catalyst. These results show the advantage of the adsorption-photodegradation mechanism resulting in

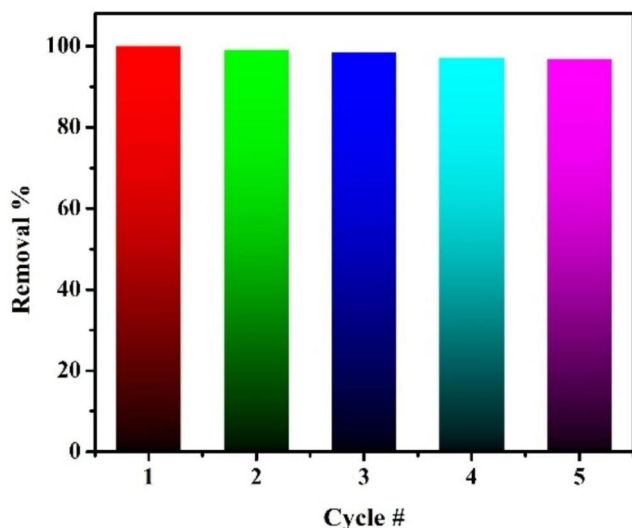


Fig. 10 Photodegradation efficiency of BTX on 20 ZF/P @ MOF-5 nanocomposites in different cycles

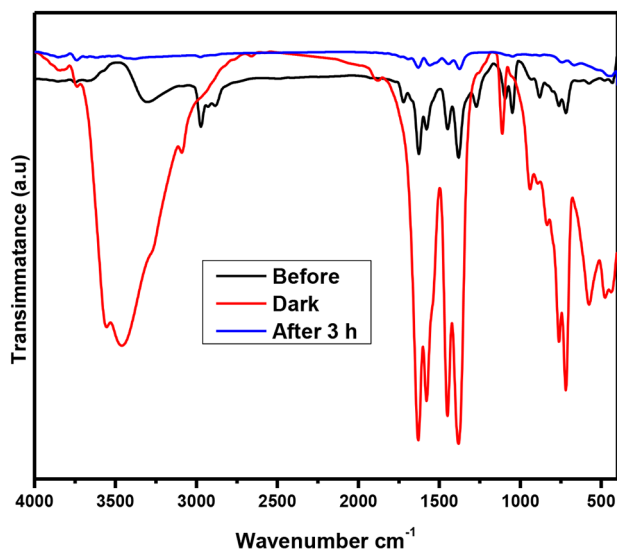


Fig. 11 FT-IR spectra of used 20P/ZF @ MOF-5

cleaning the surface of the catalyst and regenerating it for other pollutant molecules to be degraded.

4.10 The Proposed Dual Z-scheme Photocatalytic Mechanism in the CGN System

To understand the photocatalytic mechanism, the main active oxidant in the photocatalytic reaction process should be identified. The oxidants generated in the photocatalytic process can be measured through the addition of scavenging reagents. *p*-benzoquinone (BZQ), Isopropyl alcohol (IPA), and NaHCO_3 , are used to trap the superoxide radical ($\cdot\text{O}_2^-$), the hydroxyl radical ($\cdot\text{OH}$), and the hole (h_{VB^+}), respectively. The results in Fig. 12 show that the degradation rate

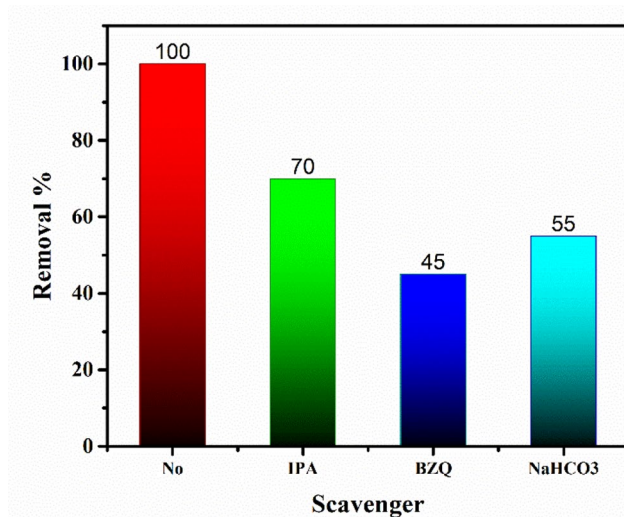


Fig. 12 Trapping experiment of reactive species hydroxide radicals, superoxide radicals, and holes, using IPA, BZQ, and NaHCO_3 , respectively, during the photocatalytic reaction on 20P/ZF @ MOF-5 composite

of BTX was decelerated after the addition of 1mM BZQ, 0.1 M IPA, and 0.1 M NaHCO_3 in the current photocatalytic system, implying that the and superoxide radicals ($\cdot\text{O}_2^-$), hydroxyl radicals ($\cdot\text{OH}$), and holes (h_{VB^+}) are the major active species responsible for the oxidation of BTX in the photocatalytic process.

Based on these results, the improved efficiency of the synthesized materials may be explained based on the creation of heterojunction between the semiconductors. As the composite material has superior visible light absorption and efficient charge carrier separation, the decomposition of BTX in visible light can be credited to a double Z-scheme mechanism. Theoretically, after exposure to light, the semiconductors' CB and VB yield the photogenerated e^-/h^+ pairs, respectively. The exact position of the valance band (VB) and conduction band (CB) edges of ZF, P and MOF-5 materials formula can be calculated [68]. The CB and VB edge potential positions of ZF are calculated to be -1.54 and $+0.38$ eV, P are -0.29 , 2.9 eV, and MOF-5 are 0.14 , 3.3 eV, respectively. It is evident that, ZF has more negative CB and VB edge potential positions than P and MOF-5. According to the above values of CB and VB Double Z-scheme heterostructure can be suggested (Fig. 13). The photogenerated e^- present in the CB of ZF displays a more negative potential than the standard reduction potential required to reduce the dissolved O_2 to $\cdot\text{O}_2^-$ radicals, which contributes in oxidizing the BTX. Though, the generated e^- in the CB of P and MOF-5 tends to bind to the h^+ in the VB of ZF. The h^+_{VB} of P and MOF-5 directly oxidize the BTX molecules to small by-products or absorb $\text{H}_2\text{O}/\text{OH}$ molecules generating $\cdot\text{OH}$ which can oxidize BTX. Therefore, the

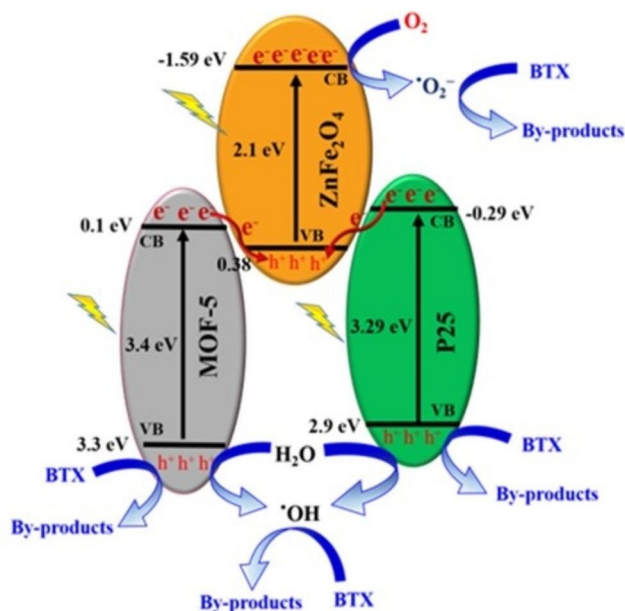


Fig. 13 Schematic diagram of double Z-scheme heterostructure

photocatalytic reaction of the developed ternary composite follows the dual Z-scheme mechanism. Table 1 illustrates a comparative analysis between the findings of this study and those reported in the existing literature.

5 Conclusion

A green method using plastic waste successfully synthesized a highly crystalline heterogeneous MOF-5 catalyst. This paper outlined the influence of 0.01wt% ZF/P incorporated in MOF-5 to form P/ZF@MOF-5 composite (with different weight ratios of ZF:P). The integrated

adsorption-photocatalysis mechanism was used for the illumination of BTX in an aqueous solution. Various physicochemical techniques, such as FTIR, SEM, TEM, XRD, characterized these catalysts BET, EDS, UV-vis., PL and XPS. Different weight ratios of ZF/P incorporated MOF-5 nanocomposite catalysts offered a reduction in the rate of electron-hole recombination and enhancement in photocatalytic activity. The prepared 20P/ZF@MOF-5 mesoporous heterogeneous adsorbent-photocatalyst presented the highest adsorption and complete photodegradation (100%) of BTX in the presence of visible radiations after 60 min. It was confirmed that the photocatalytic activity of the developed ternary composite followed the dual Z-scheme mechanism.

Supplementary Information The online version contains supplementary material available at <https://doi.org/10.1007/s10904-023-02917-0>.

Acknowledgements This paper is based upon work supported by the Science, Technology & Innovation Funding Authority (STDF) under grant number (43633).

Author Contributions All authors have equal contributions.

Funding Open access funding provided by The Science, Technology & Innovation Funding Authority (STDF) in cooperation with The Egyptian Knowledge Bank (EKB).

Declarations

Competing Interests The authors declare no competing interests.

Open Access This article is licensed under a Creative Commons Attribution 4.0 International License, which permits use, sharing, adaptation, distribution and reproduction in any medium or format, as long as you give appropriate credit to the original author(s) and the source, provide a link to the Creative Commons licence, and indicate if changes were made. The images or other third party material in this

Table 1 Summarizes numerous articles focused on the photodegradation of BTX pollutants

Catalyst	Pollutants	Irradiation conditions	Efficiency	Ref.
A. niger cells-ZnS	BTX (100 mg/L)	UV-A light source (DuraBulb UV of 4 W)	100% (60 min)	[69]
ZnO, SnO ₂ and WO ₃ (90:7:3)	BTX (1000 ppm) + (10 ppm H ₂ O ₂)	UV lamp	72.32% (210 min)	[70]
La, S, N/TiO ₂	BTX (50 mg L ⁻¹ + bias potential 1.2 V)	400 W visible light Osram lamp	51% (180 min)	[71]
TiO ₂	B, T, phenol, and Naphthalene 100 mg L ⁻¹	UV lamp (400 W)	93.29% (90 min)	[72]
γ-Fe ₂ O ₃	BTX (600 mg L ⁻¹)	Fluorescent lamps (45 W, 230 V, 50 Hz).	97% (90 min)	[73]
MIL-100 (Fe) MOF/MOX Homojunctions	BTXS (benzene, toluene, xylenes and styrene (10 sccm) o-xylene (25 ppm)	250 W Xenon	83.1% for o-xylene, 23% for benzene, 41% for toluene, 82% for p-xylene, 79% for m-xylene and 83% for styrene (150 min)	[74]
UiO66-NH ₂ /TiO ₂ /ZnO	BTX (0.11 g/L)	UV lamps (15 W)	90.03% (60 min)	[75]
ZnFe ₂ O ₄ /P25 @ MOF-5	BTX (10 ppm)	150 W Xenon lamp (400–480 nm, λ _{max} . 450 nm).	100% (180 min)	This work

article are included in the article's Creative Commons licence, unless indicated otherwise in a credit line to the material. If material is not included in the article's Creative Commons licence and your intended use is not permitted by statutory regulation or exceeds the permitted use, you will need to obtain permission directly from the copyright holder. To view a copy of this licence, visit <http://creativecommons.org/licenses/by/4.0/>.

References

1. A. Shawky, M. Alhaddad, R.M. Mohamed, N.S. Awwad, H.A. Ibrahim, "Magnetically separable and visible light-active Ag / NiCo₂O₄ nanorods prepared by a simple route for superior photodegradation of atrazine in water Progress in Natural Science: Materials International Magnetically separable and visible light-active Ag /," *Prog. Nat. Sci. Mater. Int.*, no. February, pp. 1–8, 2020, <https://doi.org/10.1016/j.pnsc.2020.01.021>
2. J. Iqbal et al., Nano-zerovalent manganese/biochar composite for the adsorptive and oxidative removal of Congo-red dye from aqueous solutions." *J. Hazard. Mater.* **403**, 123854 (Feb. 2021). <https://doi.org/10.1016/j.jhazmat.2020.123854>
3. B. Sarwar, A.U. Khan, T. Fazal, M. Aslam, N.A. Qaisrani, A. Ahmed, Synthesis of Novel MOF-5 based BiCoO₃ photocatalyst for the Treatment of Textile Wastewater. *Sustain.* **14**(19) (2022). <https://doi.org/10.3390/su141912885>
4. J. Al-sabahi, T. Bora, M. Al-abri, J. Dutta, Efficient visible light photocatalysis of benzene, toluene, ethylbenzene and xylene (BTEX) in aqueous solutions using supported zinc oxide nanorods, pp. 1–16, 2017
5. Y. Tao, Z.L. Cheng, K.E. Ting, X.J. Yin, "Photocatalytic Degradation of Phenol Using a Nanocatalyst: The Mechanism and Kinetics," *J. Catal.*, vol. 2013, pp. 1–6, 2013, <https://doi.org/10.1155/2013/364275>
6. Y. Yang et al., In-situ fabrication of a spherical-shaped Zn-Al hydroxalcite with BiOCl and study on its enhanced photocatalytic mechanism for perfluorooctanoic acid removal performed with a response surface methodology. *J. Hazard. Mater.* **399**, 123070 (2020). <https://doi.org/10.1016/j.jhazmat.2020.123070>
7. Y. Yang et al., Insights into the degradation mechanism of perfluorooctanoic acid under visible-light irradiation through fabricating flower-shaped Bi₅O₇/ZnO n-n heterojunction microspheres. *Chem. Eng. J.* **420**, 129934 (2021). <https://doi.org/10.1016/j.cej.2021.129934>
8. A. Chatterjee, A.K. Jana, J.K. Basu, A binary MOF of iron and copper for treating ciprofloxacin-contaminated waste water by an integrated technique of adsorption and photocatalytic degradation. *New. J. Chem.* **45**(37), 17196–17210 (2021). <https://doi.org/10.1039/D1NJ02880D>
9. Y. Wang, N. Lin, Y. Gong, R. Wang, X. Zhang, Cu–Fe embedded cross-linked 3D hydrogel for enhanced reductive removal of Cr(VI): characterization, performance, and mechanisms. *Chemosphere.* **280**, 130663 (2021). <https://doi.org/10.1016/j.chemosphere.2021.130663>
10. C.-C. Wang, X.-H. Yi, P. Wang, Powerful combination of MOFs and C₃N₄ for enhanced photocatalytic performance. *Appl. Catal. B Environ.* **247**, 24–48 (2019). <https://doi.org/10.1016/j.apcatb.2019.01.091>
11. H. Chen et al., Journal of Colloid and Interface Science visible-light-driven photocatalysis of carbon dioxide and organic pollutants by MFeO₂ (M = Li, Na, or K). *J. Colloid Interface Sci.* **601**, 758–772 (2021). <https://doi.org/10.1016/j.jcis.2021.05.156>
12. L. Karam, A. Miglio, S. Specchia, N. El Hassan, P. Massiani, J. Reboul, PET waste as organic linker source for the sustainable preparation of MOF-derived methane dry reforming catalysts. *Mater. Adv.* **2**(8), 2750–2758 (2021). <https://doi.org/10.1039/D0MA00984A>
13. N. You, X.-F. Wang, J.-Y. Li, H.-T. Fan, H. Shen, Q. Zhang, Synergistic removal of arsenic acid using adsorption and magnetic separation technique based on Fe₃O₄@ graphene nanocomposite. *J. Ind. Eng. Chem.* **70**, 346–354 (2019). <https://doi.org/10.1016/j.jiec.2018.10.035>
14. T. Yao, Y. Tan, Y. Zhou, Y. Chen, M. Xiang, Preparation of core-shell MOF-5/Bi₂WO₆ composite for the enhanced photocatalytic degradation of pollutants. *J. Solid State Chem.* **308**, 122882 (2022). <https://doi.org/10.1016/j.jssc.2022.122882>
15. M.J. Valero-Romero et al., Photocatalytic properties of TiO₂ and Fe-doped TiO₂ prepared by metal organic framework-mediated synthesis. *Chem. Eng. J.* **360**, 75–88 (2019). <https://doi.org/10.1016/j.cej.2018.11.132>
16. P.A. Vinoshia, L.A. Mely, J.E. Jeronsia, S. Krishnan, S.J. Das, Synthesis and properties of spinel ZnFe₂O₄ nanoparticles by facile co-precipitation route. *Optik (Stuttg.)*. **134**, 99–108 (2017). <https://doi.org/10.1016/j.ijleo.2017.01.018>
17. L. Li et al., Uniformly dispersed ZnFe₂O₄ nanoparticles on Nitrogen-Modified Graphene for High-Performance Supercapacitor as Electrode. *Sci. Rep.* **7**(1), 43116 (2017). <https://doi.org/10.1038/srep43116>
18. G. Lu, F. Chu, X. Huang, Y. Li, K. Liang, G. Wang, Recent advances in Metal-Organic frameworks-based materials for photocatalytic selective oxidation. *Coord. Chem. Rev.* **450**, 214240 (2022). <https://doi.org/10.1016/j.ccr.2021.214240>
19. S. Cavalcante, D. Vieira, I. Melo, Chemical Recycling: comparative study about the depolymerization of PET Waste-bottles to Obtain Terephthalic Acid, p. 78, 2020, <https://doi.org/10.3390/ecsoc-23-06650>
20. S. Ügdüler et al., Towards closed-loop recycling of multilayer and coloured PET plastic waste by alkaline hydrolysis. *Green. Chem.* **22**, 5376–5394 (2020). <https://doi.org/10.1039/D0GC00894J>
21. H.M. Kamari, M.G. Naseri, E.B. Saion, A Novel Research on Behavior of Zinc Ferrite nanoparticles in different concentration of poly(vinyl pyrrolidone) (PVP). *Metals.* **4**, 118–129 (2014). no. 210.3390/met4020118
22. C.D. Powell et al., Magnetically recoverable carbon – coated iron carbide with arsenic adsorptive removal properties. *SN Appl. Sci.* (2020). <https://doi.org/10.1007/s42452-020-03491-7>
23. A. Justo, Bulk and surface characterization of powder iron-doped titania photocatalysts, vol. **27**, pp. 3036–3042, 1992
24. B. Pal, M. Sharon, G. Nogami, Preparation and characterization of TiO₂ / Fe₂O₃ binary mixed oxides and its photocatalytic properties, vol. **59**, pp. 254–261, 1999
25. C.L. Luu, Q.T. Nguyen, S.T. Ho, T. Nguyen, Characterization of the thin layer photocatalysts TiO₂ and V₂O₅ - and Fe₂O₃ - doped TiO₂ prepared by the sol – gel method, vol. **035003**, <https://doi.org/10.1088/2043-6262/4/3/035003>
26. Z. Zhang, F. Zuo, P. Feng, Hard template synthesis of crystalline mesoporous anatase TiO₂ for photocatalytic hydrogen evolution †, pp. 2206–2212, 2010, <https://doi.org/10.1039/b921157h>
27. J.C.M. Vicentini, G.W. Subtil, D.M. de Oliveira, F. de Tavares, M.H.N.O. Scaliante, M. de Souza, Causa E Efeito E. Brazilian J. Dev. **7**(1), 2078–2100 (2021). <https://doi.org/10.34117/bjdv7n1-142>. "Mechanochemical Synthesis of Anatase-Rutile Phases At Ball Milling in Different Conditions and Its Cause and Effect on a Photo-Oxidation Process / Síntese Mecano-Química De Fases Anatômicas Na Moagem De Bolas Em Diferentes Condições E Sua
28. G. Kumar, D.T. Masram, Sustainable synthesis of MOF-5@GO nanocomposites for efficient removal of rhodamine B from Water. *ACS Omega.* **6**, 9587–9599 (2021). <https://doi.org/10.1021/acsomega.1c00143>

29. G. Kumar, D.T. Masram, Sustainable synthesis of MOF-5 @ GO nanocomposites for efficient removal of rhodamine B from Water, 2021, <https://doi.org/10.1021/acsomega.1c00143>
30. D.D. Andhare, S.A. Jadhav, M.V. Khedkar, S.B. Somvanshi, S.D. More, K.M. Jadhav, Structural and Chemical properties of ZnFe₂O₄ nanoparticles synthesised by Chemical Co-precipitation technique. *J. Phys. Conf.* **1644**(1), 12014 (2020). Ser.<https://doi.org/10.1088/1742-6596/1644/1/012014>
31. S. Velliyan, K.S. Murugesan, Synthesis and study on structural, morphological, optical properties and photocatalytic activity of CuO:Er³⁺ + photocatalysts. *Chin. J Phys.* **77**, 2425–2434 (2022). <https://doi.org/10.1016/j.cjph.2022.04.024>
32. P. Samoila et al., “Nanosized Spinel Ferrites Synthesized by Sol-Gel Autocombustion for Optimized Removal of Azo Dye from Aqueous Solution.” *J. Nanomater.*, vol. 2015, p. 713802, 2015, <https://doi.org/10.1155/2015/713802>
33. S. Bahtiar et al., Synthesis, investigation on structural and magnetic behaviors of spinel M-Ferrite [M = fe; zn; Mn] nanoparticles from Iron Sand. *IOP Conf. Ser. Mater. Sci. Eng.* **202**(1), 12052 (2017). <https://doi.org/10.1088/1757-899X/202/1/012052>
34. Z. Nazari, M.A. Taher, H. Fazelirad, A zn based metal organic framework nanocomposite: synthesis, characterization and application for preconcentration of cadmium prior to its determination by FAAS. *RSC Adv.* **7**(71), 44890–44895 (2017). <https://doi.org/10.1039/c7ra08354h>
35. T.A. Mulyati, R. Ediati, A. Rosyidah, Influence of solvothermal temperatures and times on crystallinity and morphology of MOF-5. *Indones J. Chem.* **15**(2), 101–107 (2015). <https://doi.org/10.22146/ijc.21202>
36. Ata-ur-Rehman et al., Synthesis of highly stable MOF-5@MWCNTs nanocomposite with improved hydrophobic properties. *Arab. J. Chem.* **11**(1), 26–33 (2018). <https://doi.org/10.1016/j.arabjc.2017.01.012>
37. M. Liu et al., “UlthraThin Metal–Organic Framework Nanosheets as a Gutter Layer for Flexible Composite Gas Separation Membranes,” *ACS Nano*, vol. 12, no. 11, pp. 11591–11599, Nov. 2018, <https://doi.org/10.1021/acsnano.8b06811>
38. M. Jong, H. Jin, J. Jegal, H. Sung, H. Gil, Depolymerization of PET into terephthalic acid in Neutral media catalyzed by the ZSM-5 acidic catalyst. *Chem. Eng. J.* **398**, 125655 (2020). <https://doi.org/10.1016/j.cej.2020.125655>
39. R. Roshani, A. Tadjarodi, Synthesis of ZnFe₂O₄ nanoparticles with high specific surface area for high-performance supercapacitor. *J. Mater. Sci. Mater. Electron.* **31**(24), 23025–23036 (2020). <https://doi.org/10.1007/s10854-020-04830-5>
40. M.V. Nikolic et al., Investigation of ZnFe₂O₄ spinel ferrite nanocrystalline screen-printed thick films for application in humidity sensing. *Int. J. Appl. Ceram. Technol.* **16**(3), 981–993 (May 2019). <https://doi.org/10.1111/ijac.13190>
41. A. Machin et al., Photocatalytic activity of silver-based Biomimetics composites. *Biomimetics.* **6**(1) (2021). <https://doi.org/10.3390/biomimetics6010004>
42. B. Hangai, E. Borsari, E.C. Aguiar, F.G. Garcia, E. Longo, A.Z. Simões, Superparamagnetic behaviour of zinc ferrite obtained by the microwave assisted method. *J. Mater. Sci. Mater. Electron.* **28**(14), 10772–10779 (2017). <https://doi.org/10.1007/s10854-017-6854-1>
43. B. Safizade, S.M. Masoudpanah, M. Hasheminasari, A. Ghasemi, Photocatalytic activity of BiFeO₃/ZnFe₂O₄ nanocomposites under visible light irradiation. *RSC Adv.* **8**(13), 6988–6995 (2018). <https://doi.org/10.1039/C7RA13380D>
44. D.L.A. de Faria, S. Venâncio, Silva, M.T. de Oliveira, Raman microspectroscopy of some iron oxides and oxyhydroxides. *J. Raman Spectrosc.* **28**(11), 873–878 (Nov. 1997). [https://doi.org/10.1002/\(SICI\)1097-4555\(199711\)28:11%3C873::AID-JRS177%3E3.0.CO;2-B](https://doi.org/10.1002/(SICI)1097-4555(199711)28:11%3C873::AID-JRS177%3E3.0.CO;2-B)
45. M.A. Alsaiani, N.A. Alhemiary, A. Umar, B.E. Hayden, “Growth of amorphous, anatase and rutile phase TiO₂ thin films on Pt/TiO₂/SiO₂/Si (SSTOP) substrate for resistive random access memory (ReRAM) device application,” *Ceram. Int.*, vol. 46, no. 10, Part B, pp. 16310–16320, 2020, <https://doi.org/10.1016/j.ceramint.2020.03.188>
46. P. Apopei, C. Catrinescu, C. Teodosiu, S. Royer, Mixed-phase TiO₂ photocatalysts: crystalline phase isolation and reconstruction, characterization and photocatalytic activity in the oxidation of 4-chlorophenol from aqueous effluents. *Appl. Catal. B Environ.* **160–161** (2014). <https://doi.org/10.1016/j.apcatb.2014.05.030>
47. A.H. Mady, M.L. Baynosa, D. Tuma, J.-J. Shim, Facile microwave-assisted green synthesis of Ag-ZnFe₂O₄@rGO nanocomposites for efficient removal of organic dyes under UV- and visible-light irradiation. *Appl. Catal. B Environ.* **203**, 416–427 (2017). <https://doi.org/10.1016/j.apcatb.2016.10.033>
48. M. Liu et al., UlthraThin metal-Organic Framework nanosheets as a gutter layer for flexible Composite gas separation membranes. *ACS Nano.* **12**(11), 11591–11599 (2018). <https://doi.org/10.1021/acsnano.8b06811>
49. X. Zhou et al., Template-free synthesis of hierarchical ZnFe₂O₄ yolk-shell microspheres for high-sensitivity acetone sensors. *Nanoscale.* **8**(10), 5446–5453 (2016). <https://doi.org/10.1039/C5NR06308F>
50. H. Asadevi, P. Prasannakumaran Nair, C. Kumari, R. Padmavati Amma, S.A. Khadar, S.C. Sasi, R. Raghunandan, ZnO@MOF-5 as a fluorescence ‘Turn-Off’ Sensor for Ultrasensitive Detection as well as probing of copper(II) ions. *ACS Omega.* **7**(15), 13031–13041 (2022). <https://doi.org/10.1021/acsomega.2c00416>
51. J. Shen, N. Wang, Y.G. Wang, D. Yu, X.K. Ouyang, Efficient adsorption of pb(II) from aqueous solutions by metal organic framework (Zn-BDC) coated magnetic montmorillonite. *Polym. (Basel).* **10**(12) (2018). <https://doi.org/10.3390/polym10121383>
52. X. Wang et al., An effective and selective stable metal-organic framework adsorben(Al-mof-5) for the removal of fluoride from water. *Desalin. Water Treat.* **216**, 220–231 (2021). <https://doi.org/10.5004/dwt.2021.26853>
53. G.Y. Zhang, Y.Q. Sun, D.Z. Gao, Y.Y. Xu, Quasi-cube ZnFe₂O₄ nanocrystals: hydrothermal synthesis and photocatalytic activity with TiO₂ (Degussa P25) as nanocomposite. *Mater. Res. Bull.* **45**(7), 755–760 (2010). <https://doi.org/10.1016/j.materresbull.2010.03.025>
54. M.M. Peng, U.J. Jeon, M. Ganesh, A. Aziz, R. Vinodh, Oxidation of Ethylbenzene using Nickel Oxide supported Metal Organic Framework Catalyst, vol. **35**, no. 11, pp. 3213–3218, 2014
55. Y. Chen, B. Zhai, Y. Liang, Y. Li, J. Li, Preparation of CdS/g-C₃N₄/MOF composite with enhanced visible-light photocatalytic activity for dye degradation. *J. Solid State Chem.* **274**, 32–39 (2019). <https://doi.org/10.1016/j.jssc.2019.01.038>
56. M. Zhang et al., Two pure MOF-photocatalysts readily prepared for the degradation of methylene blue dye under, pp. 4251–4258, 2018, <https://doi.org/10.1039/c8dt00156a>
57. Y. Chen, B. Zhai, Y. Liang, Y. Li, “Materials Science in Semiconductor Processing Hybrid photocatalysts using semiconductor / MOF / graphene oxide for superior photodegradation of organic pollutants under visible light,” *Mater. Sci. Semicond. Process.*, vol. 107, no. October 2019, p. 104838, 2020, <https://doi.org/10.1016/j.mssp.2019.104838>
58. V. Jeseentharani, M. George, B. Jeyaraj, A. Dayalan, K.S. Nagaraja, “Synthesis of metal ferrite (MFe₂O₄, M = Co, Cu, Mg, Ni, Zn) nanoparticles as humidity sensor materials,” *J. Exp. Nanosci.*, vol. 8, no. 3, pp. 358–370, Apr. 2013, <https://doi.org/10.1080/17458080.2012.690893>
59. A.H. Mady, M.L. Baynosa, D. Tuma, J.-J. Shim, Heterogeneous activation of peroxy monosulfate by a novel magnetic 3D γ -MnO₂@ZnFe₂O₄/rGO nanohybrid as a robust catalyst

- for phenol degradation. *Appl. Catal. B Environ.* **244**, 946–956 (2019). <https://doi.org/10.1016/j.apcatb.2018.11.086>
60. G. Zhang, Y. Sun, D. Gao, Y. Xu, Quasi-cube ZnFe₂O₄ nanocrystals: hydrothermal synthesis and photocatalytic activity with TiO₂ (Degussa P25) as nanocomposite. *Mater. Res. Bull.* **45**(7), 755–760 (2010). <https://doi.org/10.1016/j.materresbull.2010.03.025>
 61. L. Luu, N. Tri, Multifunctional Zn-MOF-74 as the gas adsorbent and photocatalyst advances in Natural sciences: Nano-science and Nanotechnology. no. July. (2020). <https://doi.org/10.1088/2043-6254/ab9d7c>
 62. J. Zhang et al., Integrated photocatalysis-adsorption-membrane separation in rotating reactor for synergistic removal of RhB. *Chemosphere.* **270**, 129424 (2021). <https://doi.org/10.1016/j.chemosphere.2020.129424>
 63. Z. Chen et al., “In-situ synthesis of biochar modified PbMoO₄: An efficient visible light-driven photocatalyst for tetracycline removal,” *Chemosphere*, vol. 284, no. November 2020, p. 131260, 2021, <https://doi.org/10.1016/j.chemosphere.2021.131260>
 64. V. Binas, V. Stefanopoulos, G. Kiriakidis, P. Papagiannakopoulos, Photocatalytic oxidation of gaseous benzene, toluene and xylene under UV and visible irradiation over Mn-doped TiO₂ nanoparticles. *J. Mater.* **5**(1), 56–65 (2019). <https://doi.org/10.1016/j.jmat.2018.12.003>
 65. L. Svečnjak, Z. Marijanović, P. Okińczyc, P.M. Kuś, I. Jerković, “Mediterranean propolis from the adriatic sea islands as a source of natural antioxidants: Comprehensive chemical biodiversity determined by GC-MS, firsatr, UHPLC-DAD-QTOF-MS, DPPH and FRAP assay,” *Antioxidants*, vol. 9, no. 4, 2020, <https://doi.org/10.3390/antiox9040337>
 66. V. Castelvetro et al., Polymer identification and specific analysis (Pisa) of microplastic total mass in sediments of the protected marine area of the meloria shoals. *Polym. (Basel)*. **13**(5), 1–18 (2021). <https://doi.org/10.3390/polym13050796>
 67. M. Kowalski, K. Kowalska, J. Wiszniowski, J. Turek-Szytow, Qualitative analysis of activated sludge using FT-IR technique. *Chem. Pap.* **72**(11), 2699–2706 (2018). <https://doi.org/10.1007/s11696-018-0514-7>
 68. V.Q. Nguyen, M.A. Mahadadalkar, A.M. Rabie, J.-J. Shim, Microwave-assisted synthesis of a Z-scheme heterojunction Ag/AgBr@BiOBr/Bi₂O₃ photocatalyst for efficient organic pollutant degradation under visible light. *Environ. Sci. Nano.* **9**(5), 1724–1737 (2022). <https://doi.org/10.1039/D1EN01166A>
 69. U. Priyanka, P.N.L. Lens, Enhanced removal of hydrocarbons BTX by light-driven aspergillus Niger ZnS nanobiohybrids. *Enzyme Microb. Technol.* **157**, 110020 (2022). <https://doi.org/10.1016/j.enzmictec.2022.110020>
 70. Z.A.M. Hir, R. Ali, W.A.W.A. Bakar, “PHOTODEGRADATION OF BENZENE-TOLUENE-XYLENE IN PETROLEUM REFINERY WASTE WATER BY ZnO/SnO₂/WO₃ AND ZNO/TiO₂/WO₃ TERNARY PHOTOCATALYSTS,” *Umtas*, no. January 2016, pp. 54–61, 2011
 71. M. Ghanbarnezhad, A. Parvareh, M.K. Moraveji, S. Jorfi, S. “La, N tri-doped TiO₂/nickel foam as efficient photoelectrode for degradation of BTX solution under visible light irradiation. *J. Photochem. Photobiol A Chem.* **431**, 114044 (2022). <https://doi.org/10.1016/j.jphotochem.2022.114044>
 72. I. Ul haq, W. Ahmad, I. Ahmad, M. Yaseen, Photocatalytic oxidative degradation of hydrocarbon pollutants in refinery wastewater using TiO₂ as catalyst. *Water Environ. Res.* **92**(12), 2086–2094 (2020). <https://doi.org/10.1002/wer.1370>
 73. Z. Sheikholeslami, D.Y. Kebria, F. Qaderi, Investigation of photocatalytic degradation of BTEX in produced water using γ -Fe₂O₃ nanoparticle. *J. Therm. Anal. Calorim.* **135**(3), 1617–1627 (2019). <https://doi.org/10.1007/s10973-018-7381-x>
 74. L. Chen et al., One-pot synthesis of the MIL-100 (fe) MOF/MOX homojunctions with tunable hierarchical pores for the Photocatalytic removal of BTXS. *Appl. Catal. B Environ.* **303**, 120885 (2022). <https://doi.org/10.1016/j.apcatb.2021.120885>
 75. H. Lotfi, A. Heydarinasab, M. Mansouri, S.H. Hosseini, Kinetic modeling of removal of aromatic hydrocarbons from petroleum wastewaters by UiO-66-NH₂/TiO₂/ZnO nanocomposite. *J. Environ. Chem. Eng.* **10**(1), 107066 (2022). <https://doi.org/10.1016/j.jece.2021.107066>

Publisher's Note Springer Nature remains neutral with regard to jurisdictional claims in published maps and institutional affiliations.